Chinese Chemical Letters 33 (2022) 3797–3801

Contents lists available at ScienceDirect

Chinese Chemical Letters

journal homepage: www.elsevier.com/locate/cclet

Fluorinated inverse opal carbon nitride combined with vanadium pentoxide as a Z-scheme photocatalyst with enhanced photocatalytic activity

Ningkai Ding[a], Bin Chen[a], Liang Zhou[a,*], Lingzhi Wang[c,d], Yongdi Liu[a,b], Jinlong Zhang[c,d], Juying Lei[a,b,*]

[a] State Environmental Protection Key Laboratory of Environmental Risk Assessment and Control on Chemical Process, East China University of Science and Technology, Shanghai 200237, China
[b] Shanghai Institute of Pollution Control and Ecological Security, Shanghai 200092, China
[c] Key Laboratory for Advanced Materials and Joint International Research Laboratory of Precision Chemistry and Molecular Engineering, Feringa Nobel Prize Scientist Joint Research Center, School of Chemistry and Molecular Engineering, East China University of Science and Technology, Shanghai 200237, China
[d] Shanghai Engineering Research Center for Multi-media Environmental Catalysis and Resource Utilization, East China University of Science and Technology, Shanghai 200237, China

ARTICLE INFO

Article history:
Received 9 August 2021
Revised 5 October 2021
Accepted 13 November 2021
Available online 18 November 2021

Keywords:
Carbon nitride
Inverse opal structure
Vanadium pentoxide
Fluorinate
Organic pollutants degradation

ABSTRACT

In this work, Z-scheme V_2O_5 loaded fluorinated inverse opal carbon nitride (IO F-CN/V_2O_5) was synthesized as a product of ternary collaborative modification with heterostructure construction, element doping and inverse opal structure. The catalyst presented the highest photocatalytic activity and rate constant for degradation of typical organic pollutants Rhodamine B (RhB) and was also used for the efficient removal of antibiotics, represented by norfloxacin (NOR), sulfadiazine (SD) and levofloxacin (LVX). Characterizations confirmed its increased specific surface area, narrowed bandgap, and enhanced visible light utilization capacity. Further mechanism study including band structure study and electron paramagnetic resonance (EPR) proved the successful construction of Z-scheme heterojunction, which improved photogenerated charge carrier migration and provide sufficient free radicals for the degradation process. The combination of different modifications contributed to the synergetic improvement of removal efficiency towards different organic pollutants.

For the last few years, photocatalytic oxidation technology receives great development in the remediation of environmental pollutants [1]. All-solid-state Z-scheme heterojunction photocatalysts have gotten much attention due to its enhanced separation of photogenerated carriers and shortened charge-transfer length, contributing to the effective elimination of organic and heavy metal pollutants [2–4]. Carbon nitride (g-C_3N_4) is one of the most used semiconductor photocatalysts with narrow band gap (E_g) of 2.7 eV, low toxicity, excellent stability as well as unique electronic and optical properties [5–9]. Based on its superiority, there have been attempts to construct g-C_3N_4-based Z-scheme heterojunction photocatalysts [10,11]. However, pure g-C_3N_4 material is limited by its poor visible light absorption capacity and low photogenerated electron-hole separation efficiency [12], thus various methods are studied for further application of the material. Meanwhile, inverse opal structure has caught lots of attention due to its unique properties such as photonic band gap, slow photon effect and negative refraction effect [13–15], and the structure has been successfully applied to photocatalysts like inverse opal TiO_2 [16], Ni doped inverse opal black TiO_2 and Cds doped inverse opal WO_3 [17]. There is much potential in the study of inverse opal carbon nitride (IO CN), which is proved to be efficient in aspects like H_2O_2 production, CO_2 reduction and environmental remediation [18–20]. Recent years, element doping is often considered a simple and efficient method to modify g-C_3N_4, widening its optical response range and improving the separation efficiency of photogenerated electron-hole pairs. Metal doping (K^+ [21], Na^+ [22]) and nonmetal doping (P [23], S [24]) have been proven effective for g-C_3N_4, and besides these practices, fluorinated carbon nitride (F-CN) was also reported [25,26]. On the other hand, vanadium pentoxide (V_2O_5)

* Corresponding authors.
E-mail addresses: zhouliang@ecust.edu.cn (L. Zhou), leijuying@ecust.edu.cn (J. Lei).

https://doi.org/10.1016/j.cclet.2021.11.042
1001-8417/

is an important transition metal oxide semiconductor, which has been widely used in lithium-ion batteries, gas sensors and other fields [27,28]. In addition, V_2O_5 is a typical mid-band gap (2.3 eV) semiconductor which can absorb visible light well [29]. But still, pure V_2O_5 represents low photocatalytic activity due to the narrow visible light response range and high recombination rate of photogenerated electron-hole pairs. It is noted that the CB (0.47 eV) and VB (2.73 eV) of V_2O_5 can perfectly match the CB (−1.2 eV) and VB (1.5 eV) of g-C_3N_4 to construct heterojunction. In this way, photogenerated electrons in CB of g-C_3N_4 eventually accumulated with strong reducibility, while photogenerated holes on VB of V_2O_5 eventually accumulated with strong oxidizability.

In this work, we synthesized the Z-scheme V_2O_5 loaded fluorinated inverse opal carbon nitride (IO F-CN/V_2O_5) in which heterostructure construction and element doping were combined with the inverse opal structure to carry out ternary collaborative modification. We explored the photocatalytic degradation effect on Rhodamine B (RhB) and antibiotics as typical organic pollutants. Based on various characterizations and experiments, we explored the possible photocatalytic mechanism of the catalyst.

To better examine the photocatalytic ability of IO F-CN/V_2O_5, we also synthesized bulk carbon nitride (bulk CN), IO CN, inverse opal structure F-CN (IO F-CN) and V_2O_5 loaded bulk fluorinated CN (bulk F-CN/V_2O_5) as comparisons. SiO_2 photonic crystal as the template of inverse opal structure was prepared by a Stöber method (Text S1 in Supporting information). IO CN and bulk CN were synthesized using SiO_2 and dicyandiamide (DCDA). 0.6g of DCDA and 1.0 g of SiO_2 PC were fully grounded and heated up to 520 °C for 120 min in argon gas, then heated to 550 °C for 120 min. For the yellow powder obtained after natural cooling, 4 mol/L NH_4HF_2 solution was used for etching. After 48 h, the light-yellow sample was washed for 3 times with water and dried overnight. The sample obtained was IO CN. 0.6 g of DCDA was fully grounded and heated up to 550 °C for 360 min in air stream. The yellow sample obtained after natural cooling was bulk CN. IO F-CN and IO F-CN/V_2O_5 were synthesized based on IO CN. 0.1 g IO CN was fully dissolved in a 100 mL sodium fluoride (NaF) solution of 2.5 g/L and stirred for 24 h. The sample was washed several times with deionized water and anhydrous ethanol and dried overnight. The sample obtained was recorded as IO F-CN. Then, 0.4 g of IO F-CN and 0.0052 g of ammonium vanadate (NH_4VO_3) were mixed and calcined. The sample was heated up to 550 °C at the rate of 2 °C/min, and the temperature was kept for 1h. The sample obtained after natural cooling was IO F-CN/V_2O_5. The preparation of bulk F-CN/V_2O_5 was the same as that of IO F-CN/V_2O_5 except the replacement of IO CN with bulk CN.

To characterize the morphology and microstructure of the samples obtained, the measurements of scanning electron microscope (SEM), transmission electron microscope (TEM) and high-resolution transmission electron microscope (HRTEM) were conducted. From the SEM image in Fig. 1A, it can be observed that bulk F-CN/V_2O_5 has a block structure. Figs. 1B and C showed the SEM and TEM images of IO F-CN/V_2O_5, from which we can observe an obvious 3D ordered porous structure, and the results also showed that the fluorination doping and V_2O_5 loading did not destroy the unique 3D ordered porous structure of IO CN. From the HRTEM image in Fig. 1D, we can find a region with lattice fringe of 0.287 nm corresponding to the (400) crystal plane of V_2O_5 [30].

Nitrogen adsorption-desorption curve (BET, Micromeritics ASAP 2020) was used to obtain the specific surface area of the sample under the degassing condition of heating under 300 °C for 8 h. And Barret-Joyner-Halenda (BJH) model was used to calculate the pore volume and pore size distribution of the sample. From Fig. S1 (Supporting information), it can be observed that, on the one hand, the specific surface area of IO F-CN/V_2O_5 increased significantly compared with bulk CN and bulk F-CN/V_2O_5 thanks to the unique porous structure of inverse opal structure. On the other hand, the specific surface area of IO F-CN/V_2O_5 did not change significantly compared with IO CN, which further indicated that fluorination and V_2O_5 loading had little impact on the specific surface area of IO CN.

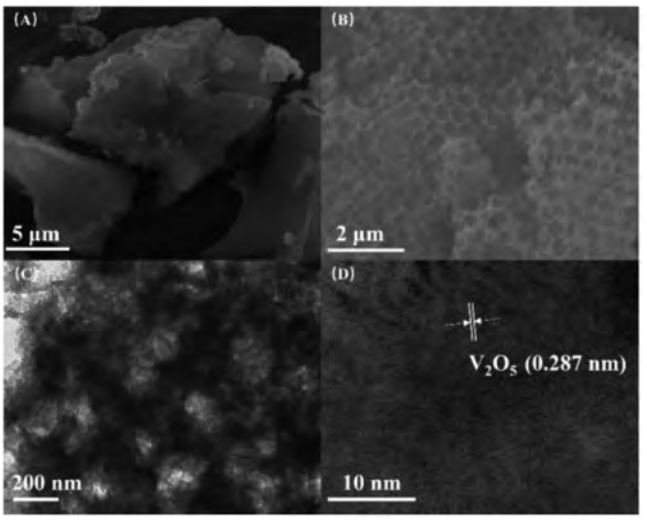

Fig. 1. (A) SEM image of bulk F-CN/V_2O_5; (B) SEM, (C) TEM and (D) HRTEM images of IO F-CN/V_2O_5.

X-ray diffractometer (XRD, Rigaku D/Max 2550 VB/PC) was used to study the crystal structure of the sample with a scanning range of 5°-80°. From Figs. 2A and B, we can clearly observe two diffraction peaks belonging to the (100) and (002) crystal planes of g-C_3N_4 at 13.0° and 27.3°, respectively. In addition, no diffraction peak belonging to NaF was found, indicating that fluorine element was successfully incorporated inside IO CN. In Fig. 2B, we can find four diffraction peaks at 20.3°, 26.1°, 31.0° and 47.3° attributed to the (001), (110), (301) and (600) crystal planes of V_2O_5 simultaneously, which are consistent with the ones of pure V_2O_5 in Fig. 2C. The results indicate that IO F-CN has successfully combined with V_2O_5 which is well-crystallized.

X-ray photoelectron spectrometer (XPS, Thermo Scientific ESCALAB 250Xi) was used to analyze the chemical composition of the sample. The results were shown in Fig. S2 (Supporting information). The internal standard was carbon and the data obtained were translated and corrected according to C 1s = 284.6 eV. Fig. S2A showed the C 1s spectrum of IO F-CN/V_2O_5, in which the peak at 288.7 eV corresponded to the existing of C-N-C bond [31], and the other peak at 284.7 eV corresponded to C-C bond [32]. Fig. S2B showed the spectrum of N 1s in which the peak of 399.1 eV corresponded to C=N−C bond, and the peaks of 400.1 eV and 401.2 eV corresponded to N−$(C)_3$ bond and N−H bond [33,34]. The O 1s of IO F-CN/V_2O_5 in Fig. S2C showed a signal peak at 532.8 eV, which belonged to the oxygen atom in the surface hydroxyl group. In F 1s, the peaks of 689.7 eV and 692.1 eV can be assigned to charge effect between fluorine atoms and π electorn system [35], proving the success of fluorination. As shown in Fig. S2E, V 2p can be decomposed into two spin orbital components at the binding energies of 517.4 eV and 524.8 eV, which were attributed to V $2p_{3/2}$ and V $2p_{1/2}$ of V_2O_5, respectively [30]. XPS results further proved the successful combination of IO F-CN and V_2O_5.

In order to explore the degradation effect for RhB, 50 mg of samples were dispersed into 50 mL of 20 mg/L RhB solution. The reaction was kept in dark condition for 20 min to ensure the adsorption balance of RhB. After 20 min, a 300 W Xenon lamp with a 420 nm cutoff filter was used for the photocatalytic process under visible light irradiation. For every 10 min during the reaction, a

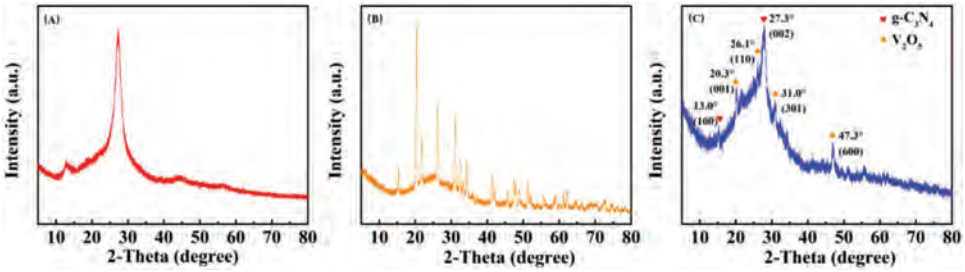

Fig. 2. XRD patterns of (A) IO F-CN, (B) IO F-CN/V_2O_5 and (C) V_2O_5.

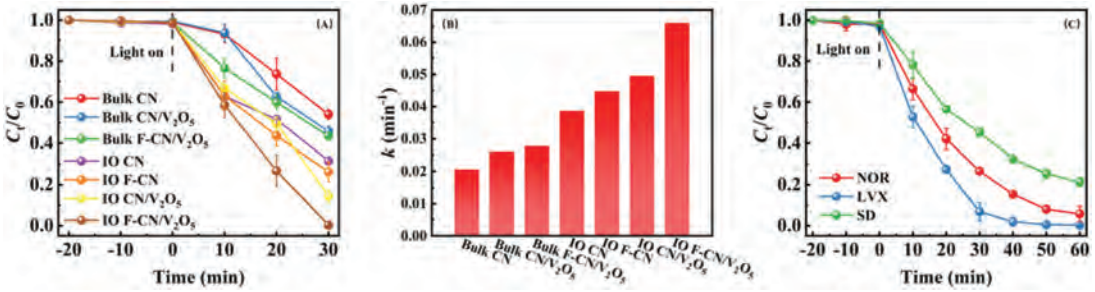

Fig. 3. (A) The degradation results to RhB over different catalysts under visible light irradiation. (B) The corresponding rate constant and (C) the degradation results of IO F-CN/V_2O_5 to NOR, LVX and SD.

certain amount of suspension was removed and centrifuged at the speed of 12000 rpm for 10 min. The absorbance of RhB at 553 nm was determined using an ultraviolet-visible spectrophotometer to determine its concentration.

The degradation of antibiotics was explored in the same method as RhB. The chosen antibiotics were norfloxacin (NOR), sulfadiazine (SD) and levofloxacin (LVX). All the antibiotics were prepared in 20 mg/L solutions. The concentration of NOR, SD and LVX was determined by HPLC (Shimadzu LC-20AD, Japan) at 7 min, 7 min and 8 min interval, respectively.

The degradation results were shown in Fig. 3A and Fig. S3 (Supporting information). Fig. 3A showed that the degradation rate of RhB for bulk CN was 48.7% after 30 min under visible light irradiation. For bulk F-CN/V_2O_5, the degradation rate of RhB was 56.9%. For IO CN, the degradation rate of RhB was 67.9%. For IO F-CN, the degradation rate of RhB was 72.4%. However, for IO F-CN/V_2O_5, the degradation rate of RhB was 100%. Fig. S3 showed the UV-vis spectra of RhB solution during the whole degradation process with IO F-CN/V_2O_5 as the catalyst. The intensity at 553 nm was significantly decreased after 30 min of visible light irradiation, and there was only a small characteristic peak at around 500 nm, which may be the possible remaining degradation intermediate while the majority of RhB was turned into H_2O and CO_2. Fig. 3A showed the degradation effect of RhB with different catalysts. The results showed that IO F-CN/V_2O_5 had the highest photocatalytic activity among all the samples. As shown in Fig. 3B, we can further compare the photocatalytic performance of bulk CN, bulk CN/V_2O_5, bulk F-CN/V_2O_5, IO CN, IO F-CN, IO CN/V_2O_5 and IO F-CN/V_2O_5 by the photocatalytic degradation rate constant (k value). The k value of IO F-CN was about 1.16 times that of IO CN, bulk F-CN/V_2O_5 was 1.07 times that of bulk CN/V_2O_5, indicating that fluorination can improve the activity of photocatalyst. In addition, the k value of IO F-CN/V_2O_5 was about 1.48 times that of IO F-CN and 1.33 times that of IO CN/V_2O_5, which showed the advantages of the combination of IO F-CN and V_2O_5 in improving the photocatalytic activity. In addition to the degradation of RhB, the catalyst IO F-CN/V_2O_5 was also used for degradation of antibiotics under visible light irradiation. As shown in Fig. 3C, after irradiation for 60 min, the degradation rate of NOR, SD and LVX (20 mg/L) was 69.6%, 80.3% and 100%, respectively. Based on the degradation results of RhB and antibiotics, the prepared IO F-CN/V_2O_5 catalyst had a good performance in degrading various organic pollutants.

The adsorption effect of catalysts was also studied. As shown in Fig. S4A (Supporting information), catalysts with inverse opal structure could adsorb more RhB under dark condition, but the total amount was only 2%-4%, which had little influence on the photocatalytic degradation process. Fig. S4B (Supporting information) showed the adsorption effect of different antibiotics with IO F-CN/V_2O_5 under dark conditions. SD could hardly be adsorbed, while 15% of NOR and LVX were adsorbed. According to the results above, it can be confirmed that most organic pollutants were removed by degradation under light irradiation rather than adsorption.

To explore the stability of the sample, cycle experiments were conducted. The results were shown in Fig. S5 (Supporting information). Fig. S5A showed that the sample remained a strong ability for RhB degradation after 4 times of use. Fig. S4B showed that the XRD pattern of IO F-CN/V_2O_5 did not change significantly after the cycle experiments, indicating that the crystal structure of the sample did not change. The SEM image in Fig. S5C and TEM image in Fig. S5D further verified that after the cycle experiments the material remained good mechanical stability. All the results above showed that the catalyst can be reused for a good practical application prospect with good stability.

To reveal the photocatalytic mechanism of the sample, a series of photochemical tests were conducted. The results were shown in Fig. S6 (Supporting information). Photoluminescence (PL) emission spectra were used to validate the photogenic carrier separation efficiency of the modified catalysts. As shown in Fig. S6A, the samples can be sorted by PL strength as follows: bulk CN > bulk F-CN/V_2O_5 > IO CN > IO F-CN > IO F-CN/V_2O_5. Therefore, the photocatalytic system of IO F-CN/V_2O_5 presented the best photogenic carrier separation ability, which explained its best photocatalytic ability in RhB degradation process. At the same time, we tested the photocurrent (Fig. S6B) and electrical impedance (Fig. S6C) of the samples. The results showed that IO F-CN/V_2O_5 got the

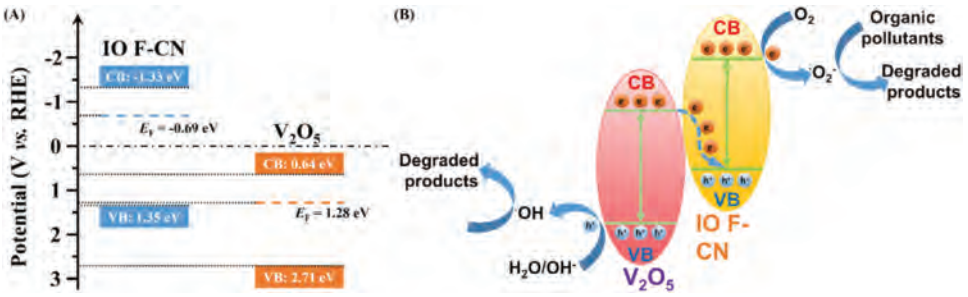

Fig. 4. (A) Schematic diagram for the band alignments of IO F-CN and V_2O_5. (B) Schematic illustration of the photocatalytic mechanism for IO F-CN/V_2O_5.

highest photocurrent intensity as well as the minimum electrical impedance, which further proved that IO F-CN/V_2O_5 had the best photogenerated carrier separation capability.

To further explore other possible reasons for the enhanced photocatalytic activity, we conducted UV-DRS tests on the sample shown in Fig. S7 (Supporting information). Fig. S7A showed that the absorption capacity of IO F-CN in visible light region was enhanced compared with IO CN, which may be related to fluorination [36]. The band gap (E_g) of the catalyst was evaluated by the Kubelka-Munk equation (Eq. 1) [37,38]:

$$\alpha h\nu = A(E_g - h\nu)^2 \quad (1)$$

Fig. S7B showed that the band gap (E_g) of IO CN and IO F-CN were 2.68 eV and 2.64 eV respectively. It can be observed that fluorination can narrow the E_g of the material to a certain extent, which was consistent with previous literature results [39]. The Mott-Schottky curves in Figs. S7C and D were used to determine the Fermi energy level (E_F) [40–42]. The exact potentials were converted into the reversible hydrogen electrode (RHE) as followed (Eq. 2):

$$E_{RHE} = E_{SCE} + 0.0591\,pH + 0.24 \quad (2)$$

Considering that the pH of Na_2SO_4 solution was 6.8, the E_F potentials of IO F-CN and V_2O_5 was −0.69 eV and 1.28 eV respectively. Thus, photogenerated electrons would transfer from V_2O_5 with higher Fermi level to IO F-CN, and XPS-VB results (Fig. S8 in support information) were used to determind the specfic band structure [43]. According to the band structure established above, the band alignment of IO F-CN and V_2O_5 was plotted in Fig. 4A.

In order to explore the main active species of the photocatalytic process and verify possible charge transfer pathways, triethanolamine (TEOA, 1 mmol/L), benzoquinone (BQ, 1 mmol/L) and thiobarbituric acid (TBA, 1 mmol/L) were used as capture agents for h^+, $^{\bullet}O_2^-$ and $^{\bullet}OH$, respectively. The procedure of free radical capture experiments was similar to that of photocatalytic degradation experiments. Fig. S9 (Supporting information) showed that BQ as the $^{\bullet}O_2^-$ trapping agent had a significant effect on the photocatalytic activity of photocatalyst, indicating that $^{\bullet}O_2^-$ was the main active substance in the photocatalytic oxidation process, while $^{\bullet}OH$ and h^+ played a relatively weaker role. The electron paramagnetic resonance (EPR) examination was also performed, validating the existence of superoxide (Fig. S10A in Supporting information) and hydroxyl radicals (Fig. S10B in Supporting information) by using 5,5-dimethyl-1-pyrroline N-oxide (DMPO) as spin-trapping agent [44,45].

Based on the experimental results above, the possible mechanism of IO F-CN/V_2O_5 photocatalytic system was clarified as follows: as shown in Fig. 4B, both IO F-CN and V_2O_5 can be excited by visible light to generate photoelectron-hole pairs. If the photoelectron-hole pairs on the charge transfer path were of the traditional type II-scheme heterojunction system, the photoelectrons in the CB of V_2O_5 will not be combined with O_2 to produce $^{\bullet}O_2^-$, for that the potential of V_2O_5 CB (0.64 eV) was more positive than standard oxidation-reduction potentials of $O_2/^{\bullet}O_2^-$ (0.33 eV *vs.* NHE). However, according to the results of the free radical capture experiment, we proved that $^{\bullet}O_2^-$ was the main active species of the reaction. Therefore, photogenerated electrons in CB of V_2O_5 tended to transfer directly to VB of IO F-CN and compound with photogenerated holes. In this way, the e^- accumulated in CB of IO F-CN with higher reducing capacity can combine with O_2 to form $^{\bullet}O_2^-$. Meanwhile, h^+ accumulated in VB of V_2O_5 can directly oxidize organic pollutants. In conclusion, the IO F-CN/V_2O_5 heterojunction prepared was verified as Z-scheme heterojunction, which can improve the separation and transfer efficiency of photogenerated electron-hole pairs effectively and showed a strong oxidation capacity to enhance the degradation capacity of organic pollutants.

In this study, IO F-CN was synthesized and combined with V_2O_5 by a hard template method and calcination as a Z-scheme heterojunction photocatalyst. Through various characterizations, it was proved that the photocatalyst had improved visible light utilization capacity and efficient photogenic carrier separation efficiency due to the synergistic effect of fluorination and V_2O_5. The material was applied to the photocatalytic degradation of organic pollutants represented by RhB and antibiotics, and the results exhibited its excellent photocatalytic activity. The photocatalytic degradation rate constants of RhB are 3.2 times and 1.7 times higher than that of bulk CN and IO CN respectively, indicating the synergistic effect of element doping, heterostructure construction alongside with inverse opal structure in the photocatalytic process. The free radical capture experiments showed that the main active species of the degradation system was $^{\bullet}O_2^-$. In addition, the material had a good cyclic stability.

Declaration of competing interest

The authors declare that they have no known competing financial interests or personal relationships that could have appeared to influence the work reported in this paper.

Acknowledgments

The authors are grateful for support from the National Natural Science Foundation of China (Nos. 21777044 and 22076046, 22176061), the Science and Technology Commission of Shanghai Municipality (Nos. 19ZR1472400, 19230711300 and 20DZ2250400).

Supplementary materials

Supplementary material associated with this article can be found, in the online version, at doi:10.1016/j.cclet.2021.11.042.

References

[1] Y. Ye, Z. Zang, T. Zhou, et al., J. Catal. 357 (2018) 100–107.
[2] D. Yuan, M. Sun, S. Tang, et al., Chin. Chem. Lett. 31 (2020) 547–550.

[3] Y.C. Zhou, P. Wang, H. Fu, C. Zhao, C.C. Wang, Chin. Chem. Lett. 31 (2020) 2645–2650.
[4] Q. Xu, L. Zhang, B. Cheng, J. Fan, J. Yu, Chem 6 (2020) 1543–1559.
[5] Y. Xing, X. Wang, S. Hao, et al., Chin. Chem. Lett. 32 (2021) 13–20.
[6] J. Fu, J. Yu, C. Jiang, C. Bei, Adv. Energy Mater. 8 (2018) 1701503.
[7] F. Wang, Y. Wang, Y. Feng, et al., Appl. Catal. B: Environ 221 (2017) 510–520.
[8] J. Hu, W. Cheng, S. Huang, D. Wu, X. Zhi, Appl. Phys. Lett. 89 (2006) 841–853.
[9] A. Pisanu, A. Speltini, B. Vigani, et al., Dalton Trans. 47 (2018) 6772–6778.
[10] M. Ding, J. Zhou, H. Yang, et al., Chin. Chem. Lett. 31 (2020) 71–76.
[11] B. Li, L.C. Nengzi, R. Guo, et al., Chin. Chem. Lett. 31 (2020) 2705–2711.
[12] W. Ong, L. Tan, Y. Ng, S. Yong, S. Chai, Chem. Rev. 116 (2016) 7159–7329.
[13] E.R. Brown, C.D. Parker, E. Yablonovitch, J. Opt. Soc. Am. B 10 (1993) 404–407.
[14] M. Curti, C.B. Mendive, M.A. Grela, D.W. Bahnemann, Mater. Res. Bull. 91 (2017) 155–165.
[15] E. Cubukcu, K. Aydin, E. Ozbay, S. Foteinopoulou, C.M. Soukoulis, Nature 423 (2003) 604–605.
[16] M. Wu, J. Liu, J. Jin, et al., Appl. Catal. B-Environ 150 (2014) 411–420.
[17] Y.Z. Dong, Y.S. Xue, W.W. Yang, H.M. You, Y.Su, Colloids Surf. A 561 (2019) 381–387.
[18] X. Huang, W. Gu, S. Hu, et al., Catal. Sci. Technol 10 (2020) 3694–3700.
[19] S. Lin, N. Zhang, F. Wang, et al., ACS Sustain. Chem. Eng. 9 (2021) 481–488.
[20] Y. Tian, L. Zhou, Q. Zhu, et al., Nanoscale 11 (2019) 20638–20647.
[21] S. Hu, F. Li, Z. Fan, et al., Dalton Trans. 44 (2015) 1084–1092.
[22] J. Zhang, S. Hu, Y. Wang, RSC Adv. 4 (2014) 62912–62919.
[23] D.H. Lan, H.T. Wang, L. Chen, C.T. Au, S.F. Yin, Carbon 100 (2016) 81–89.
[24] G. Liu, P. Niu, C. Sun, et al., J. Am. Chem. Soc. 132 (2010) 11642–11648.
[25] M. Xue, G. Tan, T. Liu, et al., Appl. Catal. A 578 (2019) 89–97.
[26] F. Ma, C. Sun, Y. Shao, et al., New J. Chem. 41 (2017) 3061–3067.
[27] A.D. Raj, T. Pazhanivel, P.S. Kumar, D. Mangalaraj, N. Ponpandian, Curr. Appl. Phys. 10 (2010) 531–537.
[28] C. Wang, L. Zhang, M. Al-Mamun, et al., Adv. Energy Mater. 9 (2019) 1900909.
[29] J. Su, X.X. Zou, G.D. Li, et al., J. Phys. Chem. C 115 (2011) 8064–8071.
[30] Y. Hong, Y. Jiang, C. Li, et al., Appl. Catal. B: Environ. 180 (2016) 663–673.
[31] S.C. Yan, Z.S. Li, Z.G. Zou, Langmuir 26 (2010) 3894–3901.
[32] A.P. Dementjev, A.D. Graaf, M.C.M van de Sanden, et al., Diamond Relat. Mater. 9 (2000) 1904–1907.
[33] A. Vinu, Adv. Funct. Mater. 18 (2008) 816–827.
[34] J. Xu, L. Zhang, R. Shi, Y. Zhu, J. Mater. Chem. A 1 (2013) 14766–14772.
[35] L. Zeng, X. Ding, Z. Sun, et al., Appl. Catal. B: Environ. 227 (2018) 276–284.
[36] L. Jiang, X. Yuan, Y. Pan, et al., Appl. Catal. B: Environ. 217 (2017) 388–406.
[37] H. Lei, Q. He, M. Wu, et al., J. Hazard. Mater. 421 (2022) 126696.
[38] H. Lei, M. Wu, F. Mo, et al., Nano Energy 78 (2020) 105290.
[39] Y. Wang, Y. Di, M. Antonietti, et al., Chem. Mater. 22 (2010) 5119–5121.
[40] C. Yao, R. Wang, Z. Wang, et al., J. Mater. Chem. A 7 (2019) 27547–27559.
[41] C. Yao, A. Yuan, Z. Wang, et al., J. Mater. Chem. A 7 (2019) 13071–13079.
[42] A. Yuan, H. Lei, Z. Wang, X. Dong, J. Colloid Interface Sci. 560 (2020) 40–49.
[43] Y. Liu, A. Yuan, Y. Xiao, H. Yu, X. Dong, Ceram. Int. 46 (2020) 16157–16165.
[44] H. Lei, M. Wu, Y. Liu, et al., Chin. Chem. Lett. 32 (2021) 2317–2321.
[45] H. Lei, M. Wu, F. Mo, et al., Environ. Sci.: Nano 8 (2021) 1398–1407.